

Influence of Systematically Changed Martensite Content on the Passive Film Properties of Austenitic Stainless Steel in Neutral Electrolyte

Ingmar Bösing^{1,*}, Ilya Bobrov², Jeremy Epp², Michael Baune¹, Jorg Thöming¹

¹ Chemical Process Engineering Group (CVT), University of Bremen, Leobener Strasse 6, 28359 Bremen, Germany

² Leibniz Institute for Materials Engineering IWT, University of Bremen, Badgasteiner Str. 3, 28359 Bremen, Germany

*E-mail: ingmar.boesing@uni-bremen.de

Received: 25 June 2019 / Accepted: 13 September 2019 / Published: 30 November 2019

The forming of austenitic stainless steel is often accompanied by a transformation of its crystalline structure into martensite. The effect of martensite content on the steel's passivation behavior is still controversially discussed. To investigate the influence of martensite content on the passive film properties we changed the microstructure of AISI304 samples by plastic deformation. Martensite content was determined by XRD measurements, while the alloy's corrosion resistance was characterized using cyclic voltammetry to measure passive current and charge densities. Passive layer properties were analyzed using electrochemical impedance spectroscopy and Mott-Schottky analysis. Systematic variations of crystalline structure revealed that a formation of a more defective passive layer can explain accelerated electrochemical dissolution at higher martensite content.

Keywords: stainless steel; cyclic voltammetry; EIS; XRD; passive films; passivity

1. INTRODUCTION

Stainless steels have become indispensable in our modern society. Applications include mechanical engineering, medical technology, aerospace and nuclear application[1,2]. This versatility is the result of specific material properties and durability which can be further enhanced by thermal and mechanical treatment. Such treatment typically leads to modifications of the steel's microstructure and thereby modifies certain properties, such as hardness and fracture toughness. Of special interest is the formation of martensitic stainless steel which shows a great hardness combined with a high toughness. These material properties can be achieved by a fast transition of the γ -Phase to the α -Phase, which can be achieved by either heat treatment or plastic deformation [1].

Microstructure, however, does not only affect the mechanical but also the electrochemical properties on the material surface. This change in electrochemical behavior is accompanied by a changed passivation behavior and thus a changed durability and resistance against corrosion. The effect of many alloying elements, like the positive effect of chrome [3, 4] or nickel [5, 6] on the corrosion behavior in general, the increased resistance against pitting corrosion through the addition of molybdenum [7] or the increased susceptibility to pitting through manganese [8] are already well understood. The effect of some microstructure changes on passivity, however, are still a matter of debate. While most researchers agree that a nano-crystalline structure improves passivity [2, 9, 10], the effect of grain size of micro to coarse grained materials is yet unclear [11]. For example, it was shown that a coarse grained material leads to a less-defective passive layer [12] but can either show worse [13] or better [14] resistance against corrosion, depending on the environment. Besides grain size effects, the influence of phase composition on corrosion, the influence of the ferrite fraction on the corrosion resistance of duplex stainless steel [15–17] and the effect of microstructure changes due to heat treatment were studied [18–20].

The effect of martensite on the corrosion resistance is still a matter of debate: Xu and Hu showed that electrochemical activity increases with martensite content, causing a lower resistance against pitting corrosion. Further, they showed that passive films of cold deformed samples passivated in NaCl containing solution consist of a high amount of corrosion products (CrCl_3) and $\text{Cr}(\text{OH})_3$ as well as $\text{Fe}(\text{OH})_3$ instead of mainly Fe_2O_3 and Cr_2O_3 which forms in passive films of undeformed samples and show better protectiveness [21]. Wang et al. also discovered a Cr_2O_3 rich passive film for untreated austenitic samples and a $\text{Cr}(\text{OH})_3$ rich film for deformed, martensitic samples [22]. In the case of nitrogen stainless steel, Fu et al. also observed an increase of hydrogen species in contrast to chrome oxides in the passive layer [23], which leads to a less protective passive film and can be at least partially attributed to the formation of martensite. While the effect of an increasing martensite phase on pitting corrosion was shown, its effect on the passive layer by crystal lattice distortion as well as its impact on general surface corrosion is still subject to debate.

In a recent study, Solomon et al. argue that deformation-induced martensite transformation of stainless steel leads to flaws in the microstructure which cause the passive film to rupture [24]. Zhang et al. investigated the corrosion properties of differently treated low-alloyed steel and could show that tempered martensite showed a higher corrosion rate compared to ferrite-bainite steel. They attributed this behavior to the higher amount of carbides formed in the martensitic steel assuming that the carbides might act as cathodic sites and accelerate the overall reactions [25]. All these reports rely on single samples with multiple changes of material characteristics during treatment, rather than on systematic variations of crystalline structure alone.

Recently, He et al. produced steel with various martensite contents (0.6%, 6%, 12% and 20%) by hot rolling. They found that pitting potential and passive film resistance decreases with martensite content up to 6%. When martensite content is further increased the pitting potential and film resistance increased as well [26]. However, in addition to the phase transformation from austenite to martensite the hot rolling process leads to a change in grain size and dislocation density. As explained above, it is absolutely necessary to take this changes into account. Both grain size and dislocation density can have a strong effect on the passive layer and might compensate each other. In an earlier study we could show that a high martensite content combined with a small grain size and high dislocation density results in

nearly the same corrosion current compared to low martensite content and large grains [27]. The underlying principles, however, of the martensite impact on the corrosion behaviour remain unclear.

Against this background, we hypothesize that the martensite content is directly related to the protectiveness of the passivation layer. In order to show this we plastically deform austenitic stainless steel samples by rotary swaging – a method that allows to systematically vary martensite contents while producing samples of same grain size [27,28]. A thorough electrochemical analysis is performed by means of cyclic voltammetry (CV), electrochemical impedance spectroscopy (EIS), and Mott-Schottky (M-S) analysis in order to reveal charge densities, passive layer properties, and defect density of the passive layer respectively. This allows us to gain deeper insight into the passivation processes of mixed austenitic/martensitic stainless steel and their resistance against corrosion.

2. METHODS

2.1. Material

The test samples were prepared from commercial AISI 304 stainless steel wires with an element distribution as shown in Table 1. Different martensite content was achieved by plastic deformation due to cold rotary swaging using different feed velocities (1, 5 and 10 mm/s). This process decreased the grain size to 2.2 μm independent of feed velocity [27]. Afterwards the samples were cut in 20 mm pieces, cast in epoxy resin and embedded in a PVC holder.

Table 1. Element distribution in commercial AISI 304 stainless steel (DIN EN 10088-3)

	C	Si	Mn	P	S	Cr	Ni	N
min.	-	-	-	-	-	17.5	8	-
max.	0.07	1.0	2.0	0.045	0.03	19.5	10.5	0.1

2.2. XRD Measurements

For the quantitative phase analysis standard X-Ray diffraction methods were used [29]. The measurements were performed using a MZ IV diffractometer (GE Inspection Technology, Ahrensburg, Germany). For signal detection a position-sensitive detector “Miostar 2” (Photron-X) was used. $K\beta$ -Filtration was carried out by using Vanadium filter. The experimental data was collected on the outer surface of the unembedded wire pieces. The measuring range of 2θ -values for all diffraction profiles in the present work was chosen from 60° to 164° degrees. The measurements were performed with a scan step of 0.05° .

Further refinement of collected data was carried out by using the software TOPAS 4.2 (Bruker AXS, Karlsruhe, Germany). The refinement algorithm is based on Rietveld method [30]. By taking into

account the instrumental contributions and the crystal structure of the present phases, including microstructural features like crystallite size and microstrains, the measured pattern is refined with a calculated pattern. The fit quality criterion is the residuals-weighted profile (weighted R-factor), R_{wp} . With increasing fit quality R_{wp} arrives at a minimal value (\geq).

$$R_{wp} = \sqrt{\frac{\sum U_i (Y_{i,obs} - Y_{i,calc})^2}{\sum (Y_{i,calc})^2}} \quad (1)$$

Here $Y_{i,obs}$ is the measured and $Y_{i,calc}$ is the calculated intensity at each 2θ position i [30]. Phase composition was refined taking into account the initial austenite phase (FCC, face-centered cubic) and deformation-induced martensite phase (BCC, body-centered cubic). Preferred orientation in $\langle 011 \rangle$ direction, as a result of rotary swaging process, was taken into account using the March-Dollase approach [31] implemented in TOPAS 4.2.

2.3. Electrochemistry

All electrochemical measurements were carried out at room temperature in a standard three electrode cell using a Metrohm Autolab potentiostat with the PGSTAT204 and the FRA32 modules. A platin electrode served as counter electrode and a Ag/AgCl electrode as reference electrode. The investigated deformed material samples act as working electrodes. All potentials in this paper are referred to the Ag/AgCl electrode.

Cyclic voltammetry (CV) measurements were performed in 0.1 M phosphate buffer solution (pH = 7.5) at room temperature to investigate the oxidation and reduction processes of the metal species. The scan rate was set to 100 mV/s, the starting potential was set to -1000 mV vs Ag/AgCl and the return potentials lie at -1000 mV vs Ag/AgCl and 1100 mV vs Ag/AgCl. Before each measurement all existing oxide layers were removed by cathodic polarization at -1100 mV vs Ag/AgCl.

The electrochemical impedance spectroscopy (EIS) were performed in the same 0.1 M phosphate buffer (pH = 7.5) after polarization at -1100 mV vs Ag/AgCl to remove any existing oxide layer and subsequent passive layer formation at open circuit potential (OCP) for 3600 s. The EIS measurements were performed at OCP in the frequency range between 10^5 Hz and 0.1 Hz with an AC amplitude of ± 10 mV_{rms}.

Mott-Schottky (M-S) measurements were performed in 0.1 M phosphate buffer after 1 h passive film formation at OCP. The M-S measurements were performed in the potential region between -0.3 V and 0.6 V by sweeping in positive direction. The measurements were obtained at 100 Hz and with an AC amplitude of ± 10 mV_{rms}.

Before each measurement the working electrodes were wet grinded with SiC grinding paper up to 2000 grid, degreased in ethanol and cleaned in an ultrasonic bath containing deionized water.

3. RESULTS AND DISCUSSION

3.1. XRD - measurements

The martensitic phase formation during plastic deformation was studied using XRD. The XRD patterns and the Rietveld refinement of the annealed and differently deformed samples show sharp and well-resolved reflections (Figure 1), which illustrate well the evolution of martensitic α -peaks and corresponding evolution of austenite γ -peaks depending on the process parameters. The increase of the α -peak correlates with the generation of deformation-induced martensite during the process. Moreover, a broadening of the diffraction peaks can be observed.

The goodness of the XRD measurement is determined by weighted R-factors R_{wp} . A low R_{wp} indicates a good agreement while the value should aim against 1. However, an R_{wp} below 7 already indicates a good agreement between calculated and obtained data. The residuals of the weighted profiles R_{wp} of the refined XRD data lay between 3.4 and 3.6 and thus show very good agreement (Table 2). Further the precision of the quantitative analysis of the phase contents is estimated to be around ± 5 wt% in the present case.

Dislocation density of the samples was calculated by:

$$\rho = \sqrt{\frac{3ke_0^2}{2.4810^{21}D^2}} \quad (2)$$

in which the microstructure parameters, such as microstrain (e_0) and volume weighted crystalline block size (D), were also obtained by the refinement method (compare experimental section). The factor k depends on the structure and is calculated to be 16.1 for FCC materials and 14.4 for BCC materials [32]. The results of the dislocation density calculations are given in Table 2. Surprisingly, the dislocation density slightly decreases with martensite content.

Table 2. Weighted R-factors (R_{wp}) and martensite contents extracted from the XRD analysis.

Sample	R_{wp}	Martensite content / wt. %	Dislocation density / cm^{-2}
1	3.57	21	1.81×10^{10}
2	3.42	35	1.61×10^{10}
3	3.67	47	1.59×10^{10}

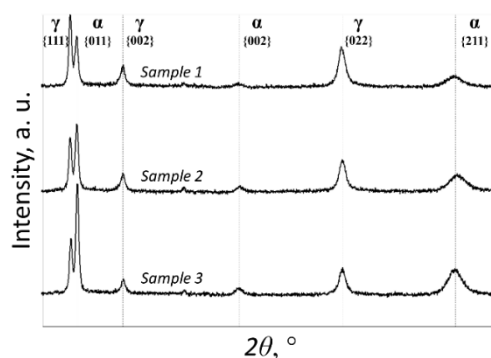


Figure 1. XRD pattern of the three different samples.

3.2. Cyclic Voltammetry

The passive layer on stainless steel is mainly composed of different iron and chrome oxides. Using CV, the formation of different oxide species can be distinguished as the formation is associated with different current density peaks. Figure 2a shows the first CV cycle of stainless steel samples with different martensite content. The observable total current density is composed of a capacitive current i_{cap} and a faradaic current i_{f} :

$$i_{\text{tot}} = i_{\text{cap}} + i_{\text{f}} \quad (3)$$

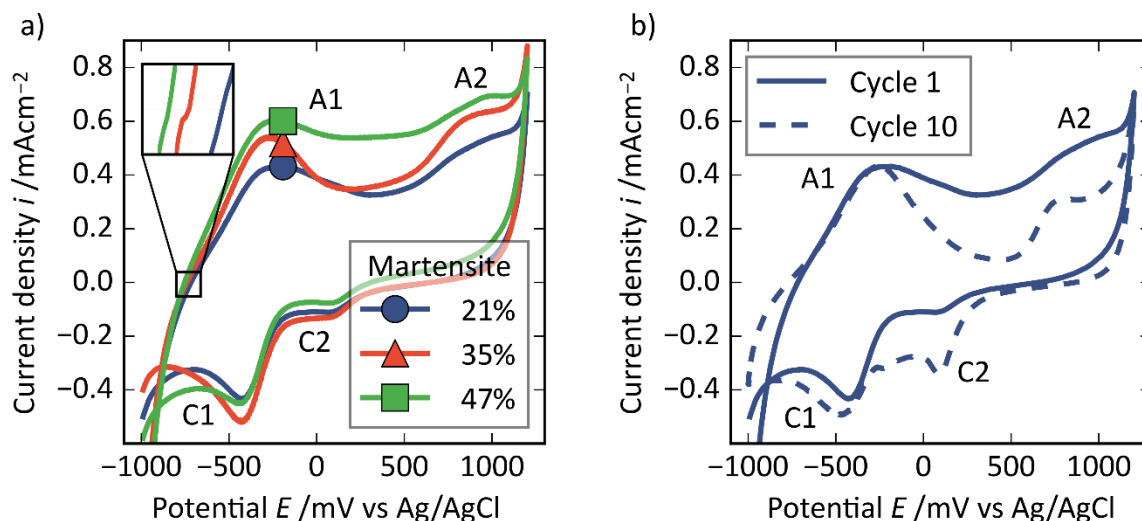


Figure 2. Cyclic voltammetry measurements in phosphate buffer at scan velocity 100 mV/s. a) First cycle of species with different martensite content, the inset shows the zero crossing. b) Cycles 1 and 10 of the 23% martensite sample.

The capacitive current density i_{cap} results from double layer charging at the electrode surface,

$$i_{\text{cap}} = C_{\text{dl}} \frac{dE}{dt} \quad (4)$$

with the change of potential over time $\frac{dE}{dt}$ (synonymous with the scan rate of the CV) and the double layer capacity C_{dl} . The scan rate is a process parameter and equal for every measurement (100 mVs^{-1}). The double layer capacity depends mainly on the electrolyte concentration (0.1 M) and the surface preparation, which is the same for all samples. Considering this, the capacitive current should be similar for all three samples and observable differences of the current density result from the faradaic processes. A high scan rate shifts the corrosion potential to more cathodic potentials [33,34] and can change the current values of the oxidation and reduction peaks in the way of more pronounced peaks [35,36]. It should be noted that, while a high scan rate is helpful for the investigation of the oxidation/reduction processes at the steel surfaces for the determination of the corrosion current and stochastic phenomena like pitting corrosion a lower scan rate should be used [33,34].

The faradaic current density i_{f} is composed of oxidation and reduction processes at the electrode surface as well as oxidation and reduction of the metal species. At high anodic and cathodic potentials (close to the return potentials) the faradaic currents are dominated by hydrogen evolution (by reduction

of water) at cathodic potentials and oxygen evolution at high anodic potentials. Additionally, the reduction of oxygen and the resulting formation of hydronium ions can occur in basic electrolyte. These processes superimpose the oxidation and reduction processes of the investigated metal species. Since these processes should be similar for every sample they can be neglected for the interpretation of the differing current densities.

While the current increases and the overall current changes from cathodic to anodic current, the oxidation of iron starts in all three samples. The first visible peak A1 was found to be the formation of Fe(III)-oxide out of Fe(II)-oxides and –hydroxides on a preexisting Cr(III)-oxide layer [37]. Due to the formation of Fe(III) oxide from Fe(II)-oxide/hydroxide, mixed species like magnetite can occur [38]. The shoulder/peak A2 indicates the oxidation of Cr(III) to soluble Cr(VI) as chromate [29, 31, 32] and the transpassive dissolution [37] and formation of oxygen.

Naturally, the back scan leads to the reduction of the oxide species on the metal surface. Firstly, the chrome oxides get reduced, associated to reduction peak C2. Since Cr(VI) is soluble the peak C2 is very small in the first cycle. With increasing number of cycles C2 becomes more pronounced because Cr(VI) remain arrested in the passive layer [41]. The reduction of Cr(VI) is followed by the reduction of the iron oxides and change of oxide states (reduction peak C1) [42]. The course of the CVs is in very good agreement with similar CVs in neutral and basic electrolytes [35,36,39,43–45].

Ongoing redox cycles alter some of the reactions in a different way. This can be seen by comparing the first and the tenth cycle (Figure 2b). While the maximum anodic peak current density remains the same for peak A1, the peak area gets tighter and the passive area becomes clearer. During the first cycle, the Cr(VI) species dissolve to the solution. Then, the peak is less pronounced and the current density increases further with increasing potential. With increasing number of cycles the chromate species are fixed inside the passive layer and the peak A2 becomes more pronounced. The decrease of the current density between peak A1 and A2 indicates a better passivation and less dissolution with increasing number of cycles.

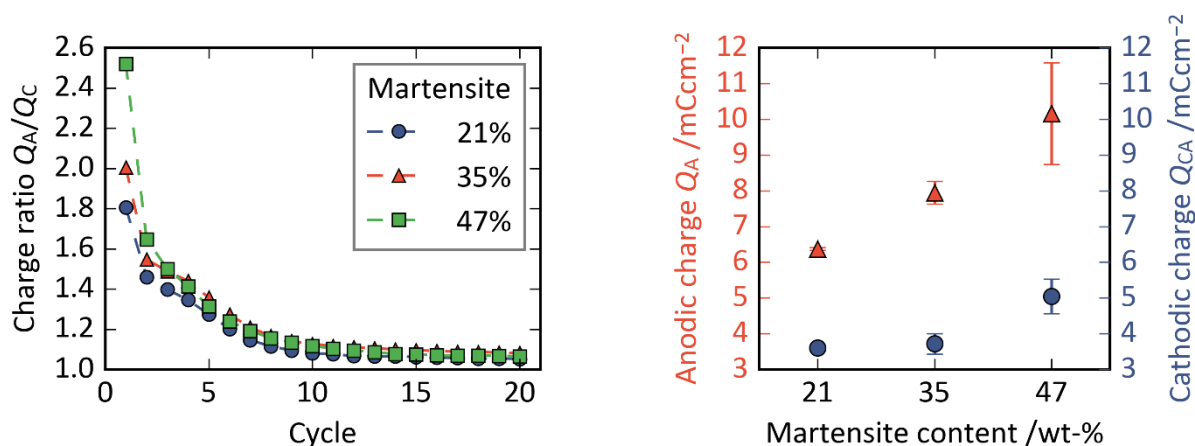


Figure 3. Faradaic charge for 3 different martensite contents: (a) Total charge ratio for all 20 cycles and (b) anodic (triangles) and cathodic (circles) charges after voltammetric cycle 1

While the qualitative trend of the CVs is similar for all three species, there are several differences due to the change in martensite content. The current density in the passive area (between peak A1 and A2) as well as the maximum peak current densities increase with increasing martensite content. This indicates a worse passivation with increasing martensite content since the passive current is an indicator for the protective effect of the passive layer.

Additional to the differences in current density one can observe differences in the zero crossing potential (inset in Figure 2a). This potential is related to the corrosion potential postponed by the capacitive current [34]. The zero-crossing potential increases with decreasing martensite content from -752.8 mV vs Ag/AgCl for the sample with martensite content of 47% over -738.7 mV vs Ag/AgCl to -717.0 mV vs Ag/AgCl for the sample with a martensite content of 21%. This underpins that the martensite phase is less noble compared to the austenite phase considering the corrosion potential being a mixed potential of both phases.

The ratio between anodic and cathodic peak area can also be used to investigate the passivation processes of the electrodes. A high peak charge ratio $\frac{Q_A}{Q_C}$ indicates an incomplete reduction of the oxidized species to their initial state during the back scan. Either the oxidation products do not remain on the surface or they remain on the surface but are not completely reduced to their initial state. If the anodic and cathodic charge densities adjust all oxidized species remain on the surface and will be reduced during the back scan. The chrome oxides get “arrested” on the electrode surface with increasing number of cycles—visible by the increasing reduction peak C2—and form a more protective and stable passive film [41].

Figure 3a shows the ratio of anodic and cathodic charge of a full cycle depending on the number of cycles. The amount of oxidized species increases with martensite content (increasing anodic charge) but a smaller proportion of the oxidized species remains on the electrode surface (increasing charge ratio) and does not contribute to a better passivation (increasing passive current density). Figure 3b compares the anodic and cathodic total charges of the first cycle as a function of the martensite content. The amount of both anodic charge as well as the amount of cathodic charge during the CV increases with increasing martensite content.

The analysis of the cyclic voltammograms indicates the importance of martensite content for the formation of the passive layer. With increasing martensite content (higher charge ratio), the solubility of the oxidation products and thus also the current density in the passive region increase. This indication of a worsening passivation with an increasing martensite content goes along with higher susceptibility to corrosion of the less-noble phases.

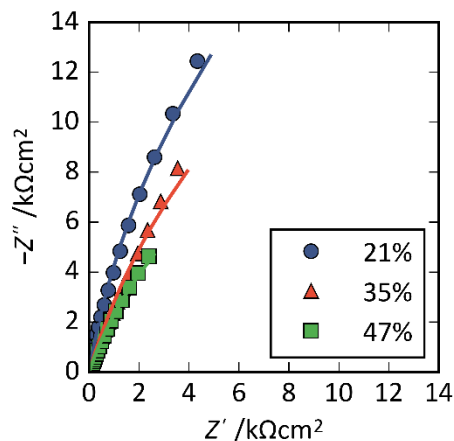


Figure 4. Bode plot of impedance data obtained in 0.1 M phosphate buffer after 1h passive layer formation at OCP; Frequency range 100 kHz - 0.1 Hz; a) Phase; b) Modulus.

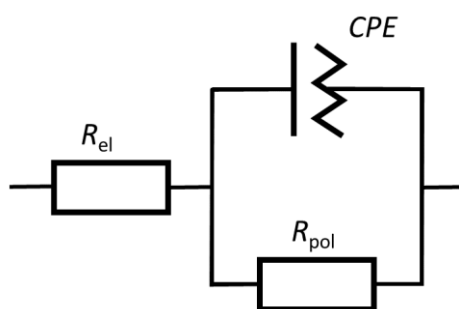


Figure 5. Equivalent electrical circuit (EEC)

3.3. Impedance Spectroscopy

Deeper insights into the nature of the passive film formed on stainless steel with differing phase composition were provided by impedance measurements at open circuit potential. Nyquist plots of impedance spectra performed in 0.1 M phosphate buffer reveal an overall impedance decrease with increasing martensite content (Figure 4a). By fitting the equivalent electric circuit (EEC) shown in Figure 5 to the impedance data, different electrical components were assigned to electrochemical counterparts on the electrode surface. The parameters proposed in the EEC represents the electrolyte resistance R_{el} , a polarization resistance R_{pol} , and the capacity of the passive layer and the electrochemical double layer CPE . To represent the capacity at the electrode surface, a constant phase element (CPE) is used. The impedance of a CPE is calculated using two variable CPE descriptors Y and N :

$$Z = \frac{1}{(j\omega)^{NY}} \quad (5)$$

For $N=1$, the CPE behaves like a perfect plate capacitor, for $N=0$, the CPE behavior represents a perfect resistor and for $N=-1$ an inductance. Any deviation from these values during EEC parameter identification when fitting the model to the EIS data indicates non-ideal behavior of the layers. This can

be expected for oxide layers that usually include inhomogeneities, and their behavior should therefore deviate from the one of perfect plate capacitors.

The EEC parameters shown in Table 3 are obtained by fitting the impedance data to the EEC model. The goodness of fit was checked by Pearson's chi squared-test showing chi-square values between $X^2 = 0.013$ and $X^2 = 0.255$, where a low number indicates a good fit.

The electrolyte resistance values for all samples are of the same order of magnitude and vary between 2.7 Ω and 3.1 Ω . The polarization resistance R_{pol} decreases with increasing martensite content indicating less resistance against the oxidation of the metal species and thus against corrosion. A similar result was found by Wang et al. who were able to observe a decreasing charge transfer resistance with increasing martensite content [22]. The CPE parameters Y and N also differ with martensite content. While N slightly decreases, the parameter Y increases with martensite content. An increase of Y which is connected to the capacity of the passive layer indicates a thinner passive film formed on the electrode surface. Since the double layer capacity of the samples should be independent from the martensite content and mainly depend on the surface treatment and the electrolyte concentration, changes of the CPE capacity can be attributed to changes of the passive layer. A connection between the CPE parameter Y of the passive film and its protective effect could already be observed for martensitic stainless steel [20]. With decreasing Y the pitting potential of the steel decreases. There are several ways for passive film breakdown which can be either connected to the bulk material itself (for example due to inclusions, depletion, grain boundaries or dislocations) or the passive film [46]. In both ways the higher martensite content seems to worsen the resistance against breakdown of passivity. Either by higher dislocation inside the bulk material or a thinner passive film. The higher metal dissolution (visible by a high oxidation current during CVs) does not necessarily lead to a thicker passive film. As stated by Wang et al. [22] and Fu et al. [23] the passive film on martensitic stainless steel consists of less Cr_2O_3 and more $Cr(OH)_3$ species. It is known that a network of connected Cr_2O_3 oxides results in good passivation of stainless steel [4]. The depletion of Cr_2O_3 in the passive film seems to accelerate the film dissolution reaction and thus leads to a thinner passive film. And it just seems natural that a thicker passive film offers more resistance to breakdown than a thinner one.

These EIS findings are in agreement with the findings of cyclic voltammetry measurements. An increasing martensite content leads to a less protective passive layer and a lower resistance against corrosion represented by the polarization resistance R_{pol} and a thinner passive layer noticeable by an increasing CPE parameter Y . Additionally the change of the CPE parameter N indicates a structural change in the passive layer. A decreasing N value shows higher deviation from the plate capacity.

Table 3. EEC parameters obtained by fitting the impedance data shown in Fig. 5 to the EEC shown in Fig. 6

Martensite content	R_{el} / ($k\Omega cm^2$)	Y / ($\Omega^{-1} cm^{-2} s^{-n}$)	N	R_{pol} / ($k\Omega cm^2$)
21%	2.92×10^{-3}	1.00×10^{-4}	0.89	72.3
35%	3.09×10^{-3}	1.32×10^{-4}	0.87	34.1
47%	2.74×10^{-3}	2.23×10^{-4}	0.80	26.5

3.4. Mott-Schottky analysis

The point-defect densities of the passive films were analyzed with Mott-Schottky analyses. By performing impedance measurements on different DC potentials it is possible to calculate the space charge capacity C_{sc} of the oxide film depending on the potential. A plot of $\frac{1}{C_{sc}^2}$ over the DC potential (Mott-Schottky plot) reveals the dopant density and the flatband potential of a semiconductor. For a linear dependency of $\frac{1}{C_{sc}^2}$ on the applied voltage E , the defect density N_D and the flat band potential E_{fb} can be calculated by the Mott-Schottky equation,

$$\frac{1}{C_{sc}^2} = \frac{2}{\epsilon \epsilon_0 e N_D} \left(E - E_{fb} - \frac{kT}{e} \right), \quad (6)$$

in which ϵ describes the permittivity of the oxide (that can be assumed as 12 for oxide layers on stainless steel [41]), ϵ_0 the permittivity of the vacuum (8.85×10^{-12} C/(Vm)), e the elementary charge of an electron (1.902×10^{-19} C), E_{fb} the flatband potential, k the Boltzmann constant (1.38×10^{-23} J/K), T the temperature, and N_D concentration of dopants. The capacity of the double layer remains nearly constant during the Mott-Schottky analysis and can be neglected [47].

By the slope of the Mott-Schottky plots in the linear region of the depletion area it is possible to determine whether the passive layer is n-doped (positive slope) or p-doped (negative slope). According to the Point Defect Model (PDM), developed in the 1980s by Macdonald et al., passive films on stainless steel are highly defect rich semiconductors [48]. Passive-film growth depends on interfacial reactions and the transport of point defects through the film. The type of the point defects inside the passive layer determines the semi-conductive nature of the oxide film. Metal interstitials and oxygen vacancies lead to n-type films while metal vacancies lead to p-type films [49].

The Mott-Schottky plots of the capacity of the space charge region within the passive layers were determined for all three samples in phosphate buffer after 1 h passive layer formation at OCP (Figure 6a). The space charge capacity was calculated at 100 Hz.

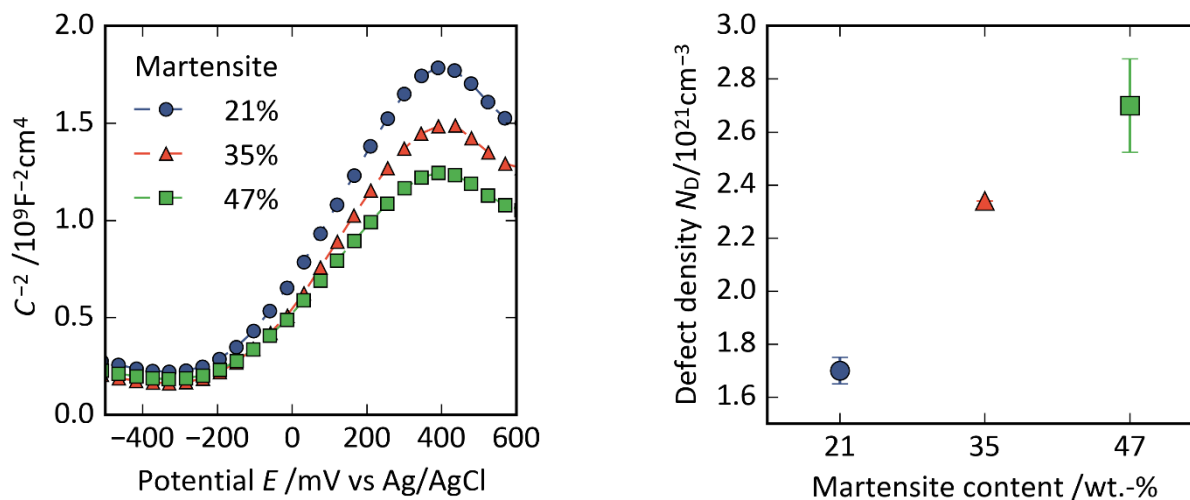


Figure 6. a) Mott-Schottky plots of the capacity of the space charge region within the passive layers obtained at 100 Hz b) Defect density of the passive layer depending on the martensite content.

The positive slope suggest the passive films formed on the surfaces of all three samples are n-type semiconductors. According to Equation 6, the dopant concentration N_D (in case of n-type passive films oxygen vacancies and metal interstitials) can be calculated by the slope of the $1/C_{sc}^2$ versus E plot. The defect density inside the passive film increases with martensite content (Figure 6b). The lattice distortions in the bulk material (the stainless steel itself) seems to accelerate the production of point defects (metal interstitials and oxygen vacancies) in contrast to regular oxides in the passive film. Distortions of the bulk material are passed on to the forming passive film as lattice defects. According to the PDM the breakdown mechanism of passive films starts with the adsorption of aggressive anions (e.g. Cl⁻) at (positive charged) oxygen vacancies [49,50]:



Here, $V_{\ddot{O}}$ indicates a two times positive charged oxygen vacancy (Kröger-Vink notation) and X^- a halide ion. A high defect density would favor the adsorption of negative charged ions at the passive film surface (due to more positive charge defects) and the injection of this defects into the passive film. Indeed Metikoš-Huković et al. could show that the change of n-type to p-type passive films can enhance the pitting corrosion resistance [51] due to less attractive sites (anion vacancies) for halide ions. The higher the defect concentration the more attractive sites to attack and the faster the breakdown of passivity due to pitting corrosion. Thus, the often observed decrease of pitting corrosion due to a higher martensite content [21–23] can be explained by the breakdown mechanism offered by the PDM and the observations of the shown Mott-Schottky analysis.

The results and interpretations of the Mott-Schottky analysis fit the EIS and CV measurements very well and underline the negative effect of a high martensite to austenite ratio for the formation of a protective passive film.

4. CONCLUSION

The electrochemical behavior of stainless steel with only varying martensite content was studied in neutral electrolyte by cyclic voltammetry, impedance spectroscopy and Mott-Schottky analysis. The results show a strong dependency of the passive layer formation (and thus the resistance against corrosion) on the martensite phase content. The measurements could reveal the following dependencies between electrochemical properties and the martensite content:

- Increasing current density in the passive area of CV measurements with increasing martensite content; indicating a higher electrochemical activity (metal dissolution) due to higher lattice distortions
- Decreasing polarization resistance with increasing martensite content, which suggests a less resistant passive layer against passivity breakdown
- Increasing passive film capacity with increasing martensite content, suggesting a thinner passive film
- Increasing defect density inside the passive film, leading to a higher number of attractive sites for anion desorption and injection into the film (start of passive film breakdown)

Increasing martensite content leads to higher electrochemical activity, apparent from higher current densities during cyclic voltammetry. A first indicator for a deteriorating passivation layer is the increasing passive current density with increasing martensite content. Additionally, the anodic to cathodic charge ratio was higher for the samples with high martensite content.

In general a high charge ratio $\frac{Q_A}{Q_C}$ means that not all oxidized species are reduced to the initial state during the back scan. This can be a result of the dissolution of the oxidized species. If the oxides dissolve, they do not entirely remain on the electrode surface and are only partly available during the back scan. Another explanation is that the oxidized species remain on the surface but is not fully reduced. Either because it is reduced to a different oxidation state (for example Fe is first oxidized to Fe^{3+} in Fe_2O_3 but reduced to Fe^{2+} in Fe_3O_4) or cannot be reduced because of bad connection to the metal surface. This could be the case in a porous layer consisting of semiconducting iron oxide particles. The porous layer has a low resistance because of its porosity (which means it is filled with electrolyte) but a high resistance between the single oxide particles. With increasing martensite content (and thus increasing charge ratio) these effects seem to increase as apparent from an increasing charge ratio $\frac{Q_A}{Q_C}$. Concluding that a higher martensite content seems to be accompanied by a higher dissolution of iron.

From impedance spectroscopy, we proposed an EEC that fit the impedance data very well. The polarization resistance decreases while the CPE capacity increases with martensite content; both indicating a thinner and less protective passive film. Mott-Schottky Analysis revealed an increasing concentration of point defects (namely oxygen vacancies and metal interstitials) in the passive layer with increasing martensite content, connected to a less stable passive layer.

It was possible to demonstrate that, isolated from other microstructure changes such as grain size, a higher martensite content leads to higher electrochemical dissolution and defect rich passive layers. This seems to be a direct result of the lattice distortions resulting from the phase transformation from

austenite to martensite [19,24] as well as due to a change in film composition [21,22]. Both effects can lead to a drastic decrease of corrosion resistance.

Understanding the influence of the crystal structure is an important step towards a comprehensive description of passivation kinetics, passive film stability and protectiveness and the crucial factors which leads to a breakdown of the layer. This understanding can be useful in an assessment of forming technologies as well as in the development of new materials.

ACKNOWLEDGEMENT

Financial support of subproject D03 “Electrochemical High Throughput Characterization of Metallic Micro Samples” and D01 “Qualification of material conditions with mechanical and physical measuring methods“ of the Collaborative Research Center SFB 1232 “Farbige Zustände” by the German Research Foundation (DFG) is gratefully acknowledged. We thank Fabio La Mantia for fruitful discussions.

DECLARATIONS OF INTEREST: None

References

1. K.H. Lo, C.H. Shek, J.K.L. Lai, *Mater. Sci. Eng. R Reports*, 65 (2009) 39–104.
2. R.K. Gupta, N. Birbilis, *Corros. Sci.*, 92 (2015) 1–15.
3. R.F. Steigerwald, *Metall. Trans.*, 5 (1974) 2265–2269.
4. K. Sieradzki, R.C. Newman, *J. Electrochem. Soc.*, 133 (1986) 1979–1980.
5. J.H. Potgieter, P.A. Olubambi, L. Cornish, C.N. Machio, E.S.M. Sherif, *Corros. Sci.*, 50 (2008) 2572–2579.
6. S.A. Távara, M.D. Chapetti, J.L. Otegui, C. Manfredi, *Int. J. Fatigue*, 23 (2001) 619–626.
7. K. Sugimoto, Y. Sawada, *Corros. Sci.*, 17 (1977) 425–445.
8. M.P. Ryan, D.E. Williams, R.J. Chater, B.M. Hutton, D.S. McPhail, *Nature*, 415 (2002) 770–774.
9. R.K. Gupta, R.K. Singh Raman, C.C. Koch, *J. Mater. Sci.*, 47 (2012) 6118–6124.
10. L. Liu, Y. Li, F. Wang, *J. Mater. Sci. Technol.*, 26 (2010) 1–14.
11. K.D. Ralston, N. Birbilis, *Corrosion*, 66 (2010) 1–4.
12. A. Fattah-Alhosseini, S. Vafaeian, *J. Alloys Compd.*, 639 (2015).
13. L. Jinlong, L. Tongxiang, W. Chen, D. Limin, *Mater. Sci. Eng. C*, 62 (2016) 558–563.
14. A. Fattah-Alhosseini, S. Vafaeian, *J. Alloys Compd.* (2015).
15. H.Y. Ha, M.H. Jang, T.H. Lee, J. Moon, *Mater. Charact.*, 106 (2015) 338–345.
16. H.Y. Ha, M.H. Jang, T.H. Lee, J. Moon, Interpretation of the Relation between Ferrite Fraction and Pitting Corrosion Resistance of Commercial 2205 Duplex Stainless Steel, Elsevier Ltd, (2014).
17. D.A. López, W.H. Schreiner, S.R.R. de Sánchez, S.. N. Simison, *Appl. Surf. Sci.*, 207 (2003) 69–85.
18. H. Hwang, Y. Park, *Mater. Trans.*, 50 (2009) 1548–1552.
19. A.F. Candelaria, C.E. Pinedo, *J. Mater. Sci.*, 22 (2003) 1151–1153.
20. I. Bösing, L. Cramer, M. Steinbacher, H.W. Zoch, J. Thöming, M. Baune, *AIP Adv.*, 9 (2019) 065317.
21. C.C. Xu, G. Hu, *Anti-Corrosion Methods Mater.*, 51 (2004) 381–388.
22. J. Wang, L.F. Zhang, *Anti-Corrosion Methods Mater.*, 64 (2017) 252–262.
23. Y. Fu, X. Wu, E.H. Han, W. Ke, K. Yang, Z. Jiang, *Electrochim. Acta*, 54 (2009) 1618–1629.

24. N. Solomon, I. Solomon, *Eng. Fail. Anal.*, 79 (2017) 865–875.
25. D. Zhang, X. Gao, G. Su, Z. Liu, N. Yang, L. Du, R.D.K. Misra, *J. Mater. Eng. Perform.*, 27 (2018) 4911–4920.
26. S. He, *Int. J. Electrochem. Sci.*, 13 (2018) 4700–4719.
27. I. Bösing, M. Herrmann, I. Bobrov, J. Thöming, B. Kuhfuss, J. Epp, M. Baune, *MATEC Web Conf.*, 04002 (2018) 1–8.
28. B. Köhler, B. Clausen, H.-W. Zoch, *Kolloquium Mikroproduktion*, BIAS Verlag, (2017).
29. J. Epp, *Mater. Charact. Using Nondestruct. Eval. Methods*, (2016), pp. 81–124.
30. G. Will, *Powder Diffraction: The Rietveld Method and the Two Stage Method to Determine and Refine Crystal Structures from Powder Diffraction Data*, (2006).
31. W.A. Dollase, *J. Appl. Crystallogr.* (1986).
32. G.K. Williamson, R.E. Smallman, *Philos. Mag.*, 1 (1956) 34–46.
33. Y. Yi, P. Cho, A. Al Zaabi, Y. Addad, C. Jang, *Corros. Sci.*, 74 (2013) 92–97.
34. X.L. Zhang, Z.H. Jiang, Z.P. Yao, Y. Song, Z.D. Wu, *Corros. Sci.*, 51 (2009) 581–587.
35. L. Veleva, M.A. Alpuche-Aviles, M.K. Graves-Brook, D.O. Wipf, *J. Electroanal. Chem.*, 537 (2002) 85–93.
36. R.A. Antunes, M.C.L. De Oliveira, I. Costa, *Mater. Corros.*, 63 (2012) 586–592.
37. S. Haupt, H.H. Strehblow, *Surf. Interface Anal.*, 21 (1994) 514–525.
38. X. Shang, *Int. J. Electrochem. Sci.*, 11 (2016) 5870–5876.
39. A. Kocijan, Č. Donik, M. Jenko, *Corros. Sci.*, 49 (2007) 2083–2098.
40. N. Ramasubramanian, *J. ...* (1985) 793–798.
41. Z. Bou-Saleh, A. Shahryari, S. Omanovic, *Thin Solid Films*, 515 (2007) 4727–4737.
42. S. Chakri, A.N. Patel, I. Frateur, F. Kanoufi, E.M.M. Sutter, T.T.M. Tran, B. Tribollet, V. Vivier, *Anal. Chem.*, 89 (2017) 5303–5310.
43. J. Morales, P. Esparza, R. Salvarezza, S. Gonzalez, *Corros. Sci.*, 33 (1992) 1645–1651.
44. S. Haupt, H.H. Strehblow, *Corros. Sci.*, 37 (1995) 43–54.
45. A. Shahryari, S. Omanovic, J.A. Szpunar, *Mater. Sci. Eng. C*, 28 (2008) 94–106.
46. P. Schmuki, *J. Solid State Electrochem.*, 6 (2002) 145–164.
47. D. Vanmaekelbergh, W.P. Gomes, *Electrochim. Acta*, 41 (1996) 967–973.
48. L.F. Lin, C.Y. Chao, D.D. Macdonald, *J. Electrochem. Soc.* (1983) 1874–1879.
49. D.D. Macdonald, *Pure Appl. Chem.*, 71 (1999).
50. D.D. Macdonald, *J. Electrochem. Soc.*, 139 (1992) 3434.
51. M. Metikoš-Huković, Z. Grubač, S. Omanovic, *J. Serbian Chem. Soc.*, 78 (2013) 2053–2067.